

# Novel Chemically Stable $\text{Ba}_3\text{Ca}_{1.18}\text{Nb}_{1.82-x}\text{Y}_x\text{O}_{9-\delta}$ Proton Conductor: Improved Proton Conductivity through Tailored Cation Ordering

Siwei Wang,<sup>†,‡</sup> Yan Chen,<sup>§</sup> Shumin Fang,<sup>†</sup> Lingling Zhang,<sup>†</sup> Ming Tang,<sup>⊥</sup> Ke An,<sup>§</sup> Kyle S. Brinkman,<sup>‡</sup> and Fanglin Chen<sup>\*†</sup>

<sup>†</sup>Department of Mechanical Engineering, University of South Carolina, Columbia, South Carolina 29208, United States

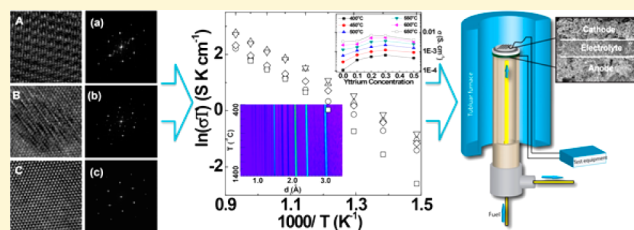
<sup>‡</sup>Department of Materials Science and Engineering, Clemson University, Clemson, South Carolina 29634, United States

<sup>§</sup>Chemical and Engineering Materials Division, Oak Ridge National Laboratory, Oak Ridge, Tennessee 37831, United States

<sup>⊥</sup>Materials Science and Technology Division, Los Alamos National Laboratory, Los Alamos, New Mexico 87545, United States

## S Supporting Information

**ABSTRACT:** Simple perovskite-structured proton conductors encounter significant challenges to simultaneously achieving excellent chemical stability and proton conductivity that are desirable for many important applications in energy conversion and storage. This work demonstrates that Y-doped complex-perovskite-structured  $\text{Ba}_3\text{Ca}_{1.18}\text{Nb}_{1.82-x}\text{Y}_x\text{O}_{9-\delta}$  materials possess both improved proton conductivity and exceptional chemical stability. Neutron powder diffraction refinement revealed a  $Fm\bar{3}m$  perovskite-structure and increased oxygen vacancy concentration due to the Y doping. High-resolution TEM analysis confirmed the perturbation of the B site cation ordering in the structure for the  $\text{Ba}_3\text{Ca}_{1.18}\text{Nb}_{1.82-x}\text{Y}_x\text{O}_{9-\delta}$  materials. Such combined effects led to improved proton conductivity with a value of  $5.3 \times 10^{-3} \text{ S cm}^{-1}$  at 600 °C for  $\text{Ba}_3\text{Ca}_{1.18}\text{Nb}_{1.52}\text{Y}_{0.3}\text{O}_{9-\delta}$  (BCNY0.3), a value 2.4 times higher compared with that of the undoped  $\text{Ba}_3\text{Ca}_{1.18}\text{Nb}_{1.82}\text{O}_{9-\delta}$ . The  $\text{Ba}_3\text{Ca}_{1.18}\text{Nb}_{1.82-x}\text{Y}_x\text{O}_{9-\delta}$  materials showed remarkable chemical stability toward water and demonstrated no observable reactions to  $\text{CO}_2$  exposure. Ionic transport number studies showed that BCNY0.3 had predominantly proton conduction below 600 °C. Solid oxide fuel cells using BCNY0.3 as an electrolyte demonstrated cell power output of  $103 \text{ mW cm}^{-2}$  at 750 °C. These results suggest that a doping strategy that tailors the cation ordering in complex perovskites provides a new direction in the search for novel proton conducting ceramics.



## 1. INTRODUCTION

Proton-conducting oxide ceramics have been extensively studied in recent years because of their high proton conductivity with low activation energy at intermediate temperatures (500–750 °C). The phenomenon of proton ionic conductivity has enabled these materials to be applied as electrolyte membranes for proton conducting solid oxide fuel cells (PC-SOFC) with lower SOFC operating temperatures, ceramic hydrogen separation membranes for high temperature applications, and electrolyte for steam electrolyzers to produce high purity hydrogen gas.<sup>1–5</sup> Of the different types of proton conducting ceramics studied, simple perovskite-structured rare-earth-doped alkaline earth based cerates (such as  $\text{BaCe}_{1-x}\text{Y}_x\text{O}_{3-\delta}$ ) have attracted considerable attention because of their highest levels of proton conductivity.<sup>6–10</sup> However, these cerates are readily decomposed in  $\text{CO}_2$  or humid atmospheres at elevated temperatures because of their inherent thermodynamic instability under such conditions.<sup>11,12</sup> Two strategies have been exploited to circumvent this problem. The first is to partially replace Ce ions with more electronegative cations such as Zr in order to form a solid (Ce, Zr) solution and improve the chemical stability.<sup>2,12,13</sup> Alkaline earth zirconates are much more stable; however, the

introduction of Zr into Ce site also greatly deteriorates the total conductivity.<sup>14,15</sup> The alternative is to explore new proton-conducting ceramics with good chemical stability while maintaining high proton conductivity. Several novel structured compounds have so far been reported as proton-conducting oxides. Acceptor-doped  $\text{LaNbO}_4$ -based orthoniobates were reported to possess pure proton conductivity at temperatures below 700 °C;<sup>16</sup>  $\beta$ - $\text{K}_2\text{SO}_4$ -structured  $\text{La}_{1-x}\text{Ba}_{1+x}\text{GaO}_{4-x/2}$  compounds containing  $\text{GaO}_4$  tetrahedral units were found to possess significant proton conductivity though they were first discovered as fast oxide-ion conductors;<sup>17</sup> perovskite-related oxygen-deficient brownmillerite-structured  $\text{Ba}_2\text{In}_2\text{O}_5$  demonstrated significant proton conductivity because of its intrinsic oxygen vacancies;<sup>18</sup> and the cation off-stoichiometric complex perovskite-structured  $\text{Ba}_3\text{Ca}_{1.18}\text{Nb}_{1.82}\text{O}_{9-\delta}$  (BCN18) showed a proton transport number close to unity in reducing atmospheres.<sup>19</sup> Although these novel structured compounds exhibited proton conduction at elevated temperatures, the proton

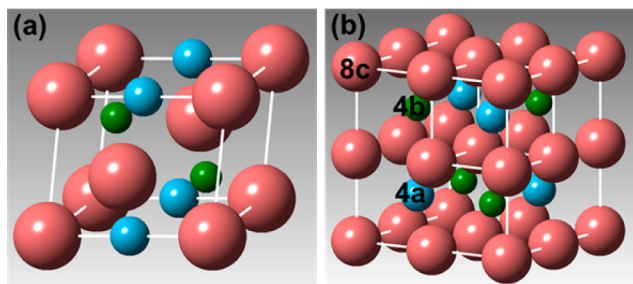
Received: November 6, 2013

Revised: January 30, 2014

conductivity values are unfortunately fairly low compared to the simple perovskite-structured proton conductors. Nevertheless, some of the novel proton conductors possess unique properties. Among them, the complex perovskite-structured BCN18 exhibits remarkable chemical and structural stability in CO<sub>2</sub> or water atmospheres.<sup>20</sup> Consequently, if the proton conductivity of BCN18 can be improved without sacrificing its chemical stability, this material could present a breakthrough in searching for new proton-conducting ceramics for important industrial applications.

Ba<sub>3</sub>Ca<sub>1.18</sub>Nb<sub>1.82</sub>O<sub>9-δ</sub> is originally derived from Ba<sub>3</sub>CaNb<sub>2</sub>O<sub>9</sub>, in accordance with the complex perovskite-structured A<sub>3</sub>B'B''O<sub>9</sub>, where one-third of the B sites are occupied by Ca<sup>2+</sup> ions, and the remaining two-thirds of the B sites are occupied by Nb<sup>5+</sup> ions. Stoichiometric Ba<sub>3</sub>CaNb<sub>2</sub>O<sub>9</sub> is 1:2 ordered for the B site cations, in which Ca<sup>2+</sup> and Nb<sup>5+</sup> ions are distributed on three planes, one plane primarily containing Ca<sup>2+</sup> and the other two planes primarily containing Nb<sup>5+</sup>, where Ca<sup>2+</sup> and Nb<sup>5+</sup> cannot move freely from B' to B'' site or vice versa.<sup>21,22</sup> Chart 1a shows the crystal structure of Ba<sub>3</sub>CaNb<sub>2</sub>O<sub>9</sub>,

**Chart 1.** (a) Crystal structure of rhombohedral Ba<sub>3</sub>CaNb<sub>2</sub>O<sub>9</sub> (*P* $\bar{3}$ *m*1), and (b) cubic Ba<sub>3</sub>Ca<sub>1.18</sub>Nb<sub>1.82</sub>O<sub>9-δ</sub> (*Fm* $\bar{3}$ *m*). Pink balls: Ba A sites. Green balls: Nb-dominant B'' sites. Blue balls: Ca rich B' sites. O atoms are not shown here for clarity

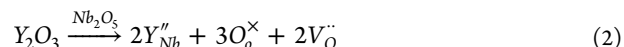


with a *P* $\bar{3}$ *m*1 space group.<sup>23</sup> Pure Ba<sub>3</sub>CaNb<sub>2</sub>O<sub>9</sub> is an insulator because no oxygen vacancies are present in the structure. In addition, the B site cation ordering blocks the movement of the ionic defects. The degree of ordering in the structure has dependence on the oxidation states and radii differences of the B site cations.<sup>24,25</sup> Because the cations of Ba<sub>3</sub>CaNb<sub>2</sub>O<sub>9</sub> cannot move freely due to the ordering, the diffusion of the oxygen vacancies will also be limited due to the substitutional ordering on the cation sublattice (cation-vacancy ordering).<sup>26</sup> To be a proton conductor, the formation of protonic defects should be created from the dissociative adsorption of water



where V<sub>O</sub><sup>··</sup> is oxygen vacancy, O<sub>O</sub><sup>×</sup> represents oxygen at the normal lattice site, and OH<sub>O</sub><sup>·</sup> is the hydroxide group indicative of formation of positively charged protonic defect. In the presence of water vapor, the concentration of protonic defects and proton conductivity can be expected to increase with an increase in oxygen vacancy concentration. The introduction of Ca<sup>2+</sup> off-stoichiometry not only creates oxygen vacancies that support significant proton conductivity but also modifies the B sites ordering. In the off-stoichiometric BCN18 with *Fm* $\bar{3}$ *m* space group, some of the B sites (4b) are occupied by ordered Nb<sup>5+</sup>, whereas the remaining Ca<sup>2+</sup> and Nb<sup>5+</sup> ions are randomly distributed in 4a sites.<sup>22</sup> The B site ordering is still present in the double perovskite BCN18 because of the unevenly distributed B' and B'' sites (Chart 1b).

It is noteworthy that the amount of oxygen vacancies may further be increased by doping with aliovalent cations in the B site. For example, a trivalent metal ion such as Y<sup>3+</sup> doped into Nb<sup>5+</sup> site would create an oxygen vacancy according to eq 2



Besides the oxygen vacancy concentration, the B sites ordering of the cations represents another factor that may influence the defect diffusions and, thus, the proton conductivity. Assuming that yttrium is doped into the B sites, the dopant Y<sup>3+</sup> with a coordination number of 6 has an ionic radius of 0.9 Å, which is situated between that of Ca<sup>2+</sup> (1.00 Å) and Nb<sup>5+</sup> (0.64 Å).<sup>27</sup> The resulting small difference in ionic radius will favor a less ordered structure. From the tolerance factor *t* for the perovskites

$$t = \frac{r_{\text{A}} + r_{\text{O}}}{\sqrt{[2(\bar{r}_{(\text{B})}) + r_{\text{O}}]}} \quad (3)$$

where *r*<sub>A</sub> and *r*<sub>O</sub> are the ionic radii of the A site cation and oxygen anion,  $\bar{r}_{(\text{B})}$  is the average radii for B site cation. For BCN18, *t* = 0.973, indicating an almost cubic structure.<sup>28</sup> The introduction of larger ionic sized Y<sup>3+</sup> (compared with Nb<sup>5+</sup>) would distort the lattice parameters while still maintaining the perovskite structure as long as *t* > 0.8. In fact, our structure refinement results indicate that introduction of Ca and Y in Ba<sub>3</sub>Ca<sub>1.18</sub>Nb<sub>1.82-*x*</sub>Y<sub>*x*</sub>O<sub>9-δ</sub> leads to a *Fm* $\bar{3}$ *m* structure (Shown in Chart 1b).

In this study, we evaluated the effect of partial substitution of Nb ions by different amount of Y ions on the crystal structure, oxygen vacancy content, ordering of the structure, and electrical conductivity for the BCN18 system. These compositional modifications were aimed at improving the proton conductivity by introducing more oxygen vacancies and tuning the cation-ordering of the system without sacrificing the chemical stability.

## 2. EXPERIMENTAL SECTION

Ba<sub>3</sub>Ca<sub>1.18</sub>Nb<sub>1.82-*x*</sub>Y<sub>*x*</sub>O<sub>9-δ</sub> (*x* = 0, 0.1, 0.2, 0.3, and 0.5, denoted as BCN18, BCNY0.1, BCNY0.2, BCNY0.3, and BCNY0.5, respectively) powders were prepared by a conventional solid state reaction method.<sup>5</sup> Starting materials BaCO<sub>3</sub> (Alfa Aesar, 99.8%), CaCO<sub>3</sub> (Alfa Aesar, 99.95%), Nb<sub>2</sub>O<sub>5</sub> (Alfa Aesar, 99.9%), and Y<sub>2</sub>O<sub>3</sub> (Alfa Aesar, 99.9%) were weighed stoichiometrically. The powders were mixed by ball-milling in ethanol for 24 h, dried, and pressed into pellets, followed by calcination at 1200 °C for 5 h in air with a heating rate of 3 °C min<sup>-1</sup>. This calcination process was repeated three times to ensure homogeneity. The final pellets were ground into powders and mixed with 5 wt % poly(vinyl alcohol) (PVA) water solution and subsequently pressed into pellets (13 mm in diameter and about 1 mm in thickness) under a uniaxial pressure of 400 MPa. The pellets were sintered at 1550 °C for 5 h in air with a heating rate of 2 °C min<sup>-1</sup>. The crystalline structures of the sintered pellets were measured using a X-ray diffractometer (Rigaku, Japan) with graphite-monochromatized Cu Kα radiation (λ = 1.5418 Å) at a scanning rate of 5° min<sup>-1</sup>. In situ high-temperature X-ray diffraction study was performed using a hot-stage-equipped Rigaku D/Max 2100 Powder X-ray Diffractometer (Cu Kα radiation). Data were collected at a 0.02° step for 2.4 s step<sup>-1</sup> over the 2θ range of 10–80°. Neutron diffraction measurement on grinded sintered powders was conducted on the time-of-flight neutron engineering materials

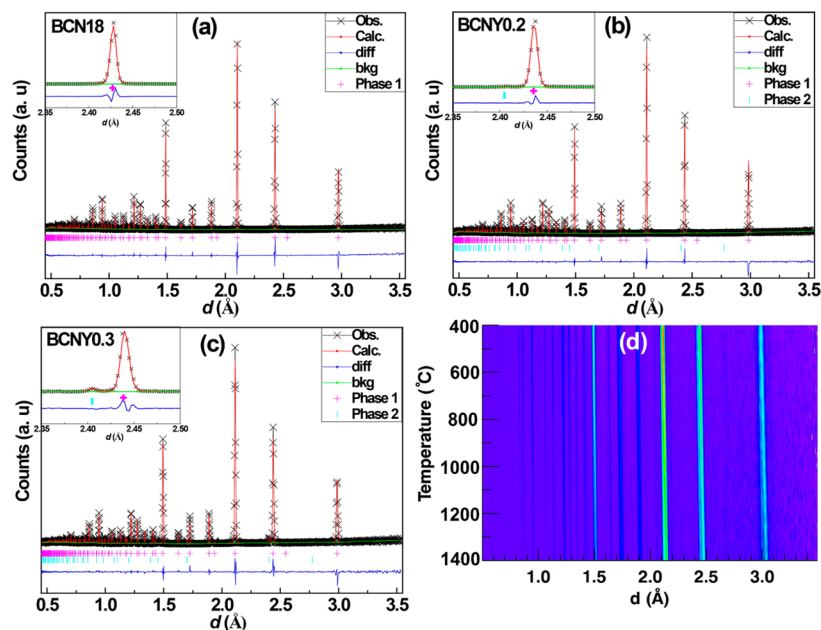


**Figure 1.** (a–c) Neutron diffraction Rietveld refinement for selected BCNY samples, (d) in situ high temperature 2D neutron diffraction pattern for sample BCNY0.3 in a vacuum furnace.

diffractometer, VULCAN, at the Spallation Neutron Source in Oak Ridge National Laboratory.<sup>29,30</sup> The diffraction patterns were analyzed by performing Rietveld refinement using General Structure Analysis System (GSAS) package and the graphical user interface (EXPGUI).<sup>31,32</sup> The X-ray photoelectron spectroscopy (XPS) measurement was employed to obtain the binding energy spectra for the samples using a Kratos Axis Ultra DLD instrument equipped with a monochromated Al  $K\alpha$  X-ray source and hemispherical analyzer. Scanning electron microscopy (SEM, FEI Quanta, and XL 30) and transmission electron microscopy (TEM, FEI Tecnai F30 Analytical, coupled with energy-dispersive X-ray spectroscopy (EDS)) were used to characterize the morphology and microstructural ordering of the samples.

For conductivity measurements, platinum paste was applied to both sides of the sintered pellets followed by baking at 950 °C for 30 min. Platinum wires were attached to the surfaces of the platinum paste. Conductivity measurements were performed using AC impedance spectra with a built-in impedance analyzer (IM6, Zahner) in a frequency range from 0.1 Hz to 8 MHz as a function of testing temperature. The sintered samples were exposed to boiling water or CO<sub>2</sub> atmosphere to test the chemical stability of the materials. As to the electrochemical open circuit voltage (OCV) tests, electrolyte-supported single cells with BCNY0.3 as an electrolyte and Pt as both electrodes were fabricated. The cell was sealed onto an alumina tube with ceramic paste (Aremco Product Inc.). Pt wires were used as the lead wire in the cell and the data were collected by the impedance analyzer. For the fuel cell demonstration, anode supported single solid oxide fuel cells using BCNY0.3 as the electrolyte, Ni-BaZr<sub>0.1</sub>Ce<sub>0.7</sub>Y<sub>0.1</sub>Yb<sub>0.1</sub>O<sub>3- $\delta$</sub>  (Ni-BZCYYb) as the anode and Ba<sub>0.9</sub>Co<sub>0.7</sub>Fe<sub>0.2</sub>Nb<sub>0.1</sub>O<sub>3- $\delta$</sub>  (BCFN) as the cathode were fabricated by two-step cosintering method as previously reported.<sup>33,34</sup> The single cell was tested with wet H<sub>2</sub> (containing 3 vol% H<sub>2</sub>O) as fuel and ambient air as oxidant. The electrochemical performances of the cells were measured using a Versa STAT3-400 electrochemical station.

### 3. RESULTS AND DISCUSSION

**3.1. Structural Characterization.** Figure 1a–c shows the neutron powder diffraction patterns of BCN18, BCNY0.2, and BCNY0.3, respectively. These diffraction patterns can be indexed and refined based on the double-perovskite-structured  $Fm\bar{3}m$  as shown in Chart 1b. According to the Rietveld refinement with trial and error, better agreement was found for the case that the Ca<sup>2+</sup> ions located at 4a sites (B' site), rather than in 4b sites (B'' site), whereas the Y<sup>3+</sup> ions distributed in both sides with exchange of Nb<sup>5+</sup> ions. The BCNY0.5 sample pellet showed secondary impurities on the surface (See Supporting Information Figure S1–S2). It was noticed that trace amount of  $Fm\bar{3}m$  structured CaO phase with lattice parameter of  $a = 4.81$  Å can be identified as the secondary phases in the Y-doped samples by the high resolution neutron diffractions, although the impurity in BCNY0.2 and BCNY0.3 could hardly be detected by XRD. This is because the large neutron beam size and the large exposed sample volume make it possible to observe a small amount of the secondary phase. Furthermore, the different neutron scattering coherent cross section of Ca (2.78 barn), Nb (6.253 barn), Y (7.55 barn), and O (4.232 barn) atoms is helpful to identify the locations and occupancies of these individual atoms and, thus, to characterize the ordering structures.<sup>35</sup> Selected structural parameters by Rietveld refinement are shown in Table 1. The lattice parameter increases with the yttrium doping level due to the larger yttrium dopants compared with the niobium ions. Sample BCNY0.2 leads to 0.325 wt % CaO precipitation, whereas BCNY0.3 results in 0.963 wt % of CaO precipitation. Although we intended to substitute Y on the Nb site, the Rietveld refinement suggested some of the doped Y may enter the Ca site resulting in trace amount of CaO segregation. In consideration of the loss of Ca, the compositions of the samples are slightly adjusted apart from the nominal compositions so that the Ca occupancy in B site accordingly matches the weight percentage of CaO while the Nb/Y ratio is maintained. The atomic occupancies for selected samples are calculated and presented in Table 1. These results indicate that the substitution of Nb<sup>5+</sup> by

**Table 1. Structural Parameters for Selected Samples by Neutron Diffraction and Rietveld Refinement**

parameters	BCN18	BCNY0.2	BCNY0.3
a (Å)	8.4368(6)	8.4077(5)	8.4473(5)
CaO wt %	0.325(42)	0	0.963(37)
$R_{wp}$	0.0491	0.0466	0.0524
$R_p$	0.0361	0.0378	0.0401
$\chi^2$	5.49	5.30	6.55
Ba 8c (0.25, 0.25, 0.25)	Uiso (Å <sup>2</sup> ) 0.01522(31)	0.01253(25)	0.01778(43)
	Occup. 1.00	1.00	1.00
Nb 4a (0, 0, 0)	Uiso (Å <sup>2</sup> ) 0.01111(64)	0.00826(39)	0.01508(90)
	Occup. 0.217(38)	0.213	0.279(56)
Ca 4a (0, 0, 0) <sup>a</sup>	Uiso (Å <sup>2</sup> ) 0.01111(64)	0.00826(39)	0.01508(90)
	Occup. 0.757(2)	0.787	0.700(2)
Y 4a (0, 0, 0)	Uiso (Å <sup>2</sup> ) 0.01111(64)		0.01508(90)
	Occup. 0.026(38)		0.022(56)
Nb 4b (0.50, 0.50, 0.50)	Uiso (Å <sup>2</sup> ) 0.00376(42)	0.00433(30)	0.00373(55)
	Occup. 0.889(38)	1.00	0.807(56)
Y 4b (0.50, 0.50, 0.50)	Uiso (Å <sup>2</sup> ) 0.00376(42)		0.00373(55)
	Occup. 0.111(38)		0.193(56)
O 24e (x, 0, 0)	x 0.2646(1)	0.2625(1)	0.2653(2)
	Uiso (Å <sup>2</sup> ) 0.02280(37)	0.02340(31)	0.02335(48)
	Occup. 0.909(2)	0.940(2)	0.911(3)
	Occup. (Cal.) 0.948	0.970	0.937

<sup>a</sup>The Ca occupancy is calculated according to the weight fraction of CaO.

$Y^{3+}/Ca^{2+}$  provides the required charge compensation from the difference in valences between  $Y^{3+}/Ca^{2+}$  and  $Nb^{5+}$ . By trial and error of the refinement, it is found that Ca will only stay in 4a site and not be allowed to be in 4b site. This result coincides with the large radii mismatch between  $Nb^{5+}$  and  $Ca^{2+}$ , which is one of the reasons for the Ca/Nb ordering structure. Although not leading to any exchange of  $Ca^{2+}$  to 4b site, the occupancy of Nb at 4b site was decreased due to the introduction of Y, which moderated the disparity of 4a and 4b sites and reduced the B site cation ordering. The oxygen occupancies for the materials are refined and presented in Table 1, with oxygen vacancy numbers of 6.0%, 9.1%, and 8.9% for BCN18, BCNY0.2, and BCNY0.3, respectively. It is noted that the actual increment of  $V_{\text{O}}$  is not as anticipated from the formulated increments based on charge neutrality due to the trace amount of segregated CaO. Our XPS results also confirmed different oxidation states for Ca 3d spectra in the samples (see Supporting Information Figure S3). It is also noted that the  $V_{\text{O}}$  contents in BCNY0.2 and BCNY0.3 are similar. This is due to the fact that the introduction of more  $Y^{3+}$  dopants into BCNY0.3 generated extra oxygen vacancies, but more  $Ca^{2+}$  loss balanced this effect. From the structure factor information, the presence of (111) and (311) peaks around 18 and 35 degrees in XRD patterns are attributed to the non-identical scattering factors of the atoms at 4a and 4b sites (see Supporting Information Figure S1), respectively. For the fully disordered perovskite, the cations at 4a and 4b sites are identical, and the (111) and (311) superlattice reflections will not be present. The intensity ratio for (111)/(220), (311)/(220), and (311)/(222) peaks can, thus, be indexed as the characteristics for the degree of B site ordering in the perovskite structure. The peak intensity ratios of selected samples are presented in Table 2.

**Table 2. Relative Intensities of Selected Peaks That Indicate the Degree of Cation Ordering of the Samples**

intensity ratio	(111)/(220)	(113)/(220)	(113)/(222)
BCN18	0.02458	0.01315	0.09456
BCNY0.3	0.02293	0.00726	0.06066
BCNY0.5	0.01680	0.00489	0.04174

It can be seen from Table 2 that as more  $Y^{3+}$  dopant is added, the relative intensities of (111) and (311) peaks are decreased, indicating a lower degree of B site cation ordering. This is expected since X-ray scattering factor is proportionally related to the atomic weight in the periodic table, and the scattering factor of Y is suited between that of Nb and Ca. The  $Y^{3+}$  doping in 4a sites (which can substitute either  $Nb^{5+}$  or  $Ca^{2+}$ ) causes a reduction of the difference in the scattering ability between 4a and 4b sites. Figure 1d shows the in situ high temperature neutron diffraction 2D contour pattern for sample BCNY0.3 tested in vacuum furnace cooling from 1400 °C down to 400 °C at a cooling rate of 3 °C min<sup>-1</sup>. The brightness change of the pattern indicates the intensity change of the neutron diffraction peaks. It can be seen that upon reducing the temperature from 1400 to 400 °C, there are only slight changes in peak intensities and d-spacing shifting due to the Debye–Waller effect and thermal expansion, respectively. There is no apparent phase transformation for BCNY0.3 during the cooling process. In situ high temperature XRD also confirmed no phase transformation from room temperature to 1000 °C (see Supporting Information Figure S4). It is believed that an oxygen atom forms two short bonds with B cations, and two long bonds with A cations in the perovskite, which means that an oxygen vacancy is more strongly trapped by a B'–O–B'' pair than by an A–O–A pair in A(B'B'')O<sub>3</sub> perovskite.<sup>36</sup> Consequently, substitution of Y for Nb perturbs or decreases the degree of ordering for oxygen vacancies in such a way that the oxygen vacancy is trapped by the Ca–O–Nb, Ca–O–Y, and Y–O–Nb pair. To check the crystal structure and the degree of cation ordering, the selected area electron diffraction (SAED) patterns and high resolution TEM (HRTEM) images were then collected for the sintered BCNY0.2 and BCNY0.3 powder samples shown in Figure 2 and Figure 3, respectively. The patterns have been indexed according to double perovskite-structure-type cell, and the lattice parameters were calculated based on the SAED patterns and TEM images. The SAED pattern of BCNY0.2 is characteristic of a typical cubic perovskite along the [111] zone axis of the sample aligned parallel to the electron beam, with calculated  $d(220) = 0.2892$  nm, consistent with the XRD and neutron powder diffraction results for the structural configuration of the sample. In addition to the Bragg reflections characteristic of the perovskite unit cell, superlattice reflections are observed (indexed by arrows in the pattern), indicating the presence of extra domains. The extra nanodomains have been confirmed by observing the corresponding HRTEM image and magnified areas shown in Figure 2iii and Figure 2A–C. The chessboard and stripe typed patterns observed are attributed to the ordering in the structure, which may be caused by displacement of atoms, by variation in the occupancy of atomic sites, or by both. In our case, it is mainly caused by the B site cation ordering due to the differences in ionic radius and charges among the  $Ca^{2+}$ ,  $Nb^{5+}$ , and  $Y^{3+}$  ions. The SAED pattern along the [100] zone axis of BCNY0.3 shows no extra spots coexisting with the ideal perovskite unit cell. However, differences in brightness of the spots are indicative of a superlattice reflection due to the ordering of the structure.<sup>37,38</sup>

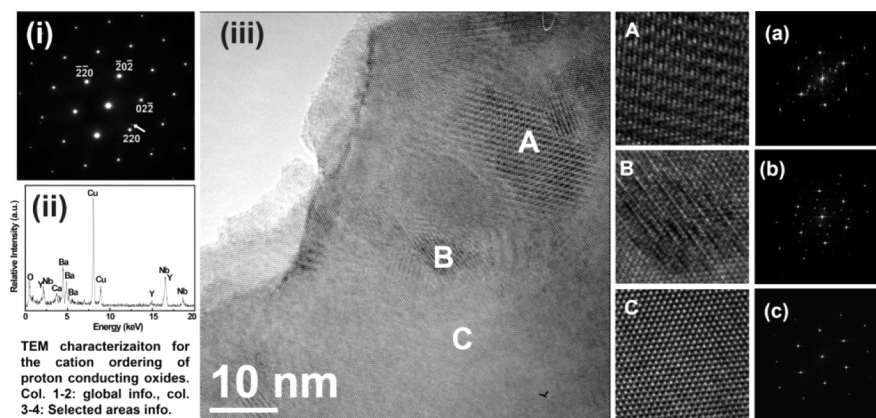


**Figure 2.** (i) SAED pattern of BCNY0.2 sintered powder along the [111] zone axis of the sample powder aligned parallel to the electron beam, (ii) EDS of the selected area, (iii) HRTEM image corresponding to the [111] zone axis of the sample, and (A–C) magnifications of A, B, C domains, respectively, and (a–c) fast Fourier transform (FFT) of the magnified domains, respectively.

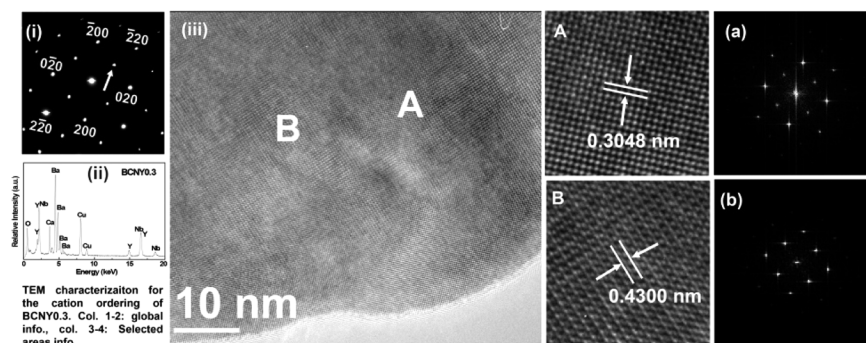


**Figure 3.** (i) SAED pattern of BCNY0.3 sintered powder along the [100] zone axis of the sample powder aligned parallel to the electron beam, (ii) EDS of the selected area, (iii) HRTEM image corresponding to the [100] zone axis of the sample, and (A–B) magnifications of A and B domains and (a–b) FFT of the magnified domains, respectively.

The reconstruction of the reciprocal space from the SAED pattern leads to a superstructure of the cell, with  $a' = \sqrt{2}/2a$  as shown in Figure 3A. The superstructure of the cell parameter is clearly observed on the HRTEM image by the domains displayed in Figure 3iii and Figure 3a. Distances of 0.4300 nm between characteristic rows of bright lines are observed in Figure 3B. If this value is transformed into that of cubic double perovskite structure, a value of 0.8600 nm is obtained, which is consistent with the lattice parameter obtained from neutron diffraction refinement. Lattice fringes in Figure 3A, indicating a  $\sqrt{2}/2$  value (0.3048 nm) of that in Figure 3B periodicity along this direction, is a reflection of ordering in the A area. The EDS nanoanalysis performed on the crystal areas in STEM mode did not show differences in the chemical composition between domains of the crystals as shown in Figure 2ii and Figure 3ii, with more Y and less Nb concentrations in BCNY0.3 samples. It is noted that for fully ordered complex perovskites, such as fully B-site-ordered  $\text{Sr}_3\text{Ca}_{1.18}\text{Nb}_{1.82}\text{O}_{9-\delta}$ <sup>39</sup> and A site and B site doubly ordered complex perovskite  $\text{KLaMnWO}_6$ ,<sup>40</sup> they show clearly ordered and even chessboard patterned TEM images and superlattice reflections in SAED patterns. It is believed that the cation ordering of the structures will reasonably result in oxygen vacancy domains of ordered clusters, which nucleate at dopant ions with negative charges to form defect associates/complexes in the structure (such as the potential  $\text{V}_{\text{O}}''\text{Y}_{\text{Nb}}''$  defect complex in our material system).<sup>36</sup> Therefore, a lower degree of cation ordering for the Y-doped samples leads to oxygen vacancy disordering, which should be beneficial for ionic transport in these material systems.

**3.2. Electrical Conductivity.** For the electrical conductivity tests, the sample surfaces were polished to remove the surface impurities before applying Pt paste on the surfaces of the samples for electrical measurement. The conductivity is obtained from the Nyquist plots of the AC impedance spectra for the samples (see Supporting Information Figure S6). Figure 4 shows the Arrhenius plot of the conductivities obtained from

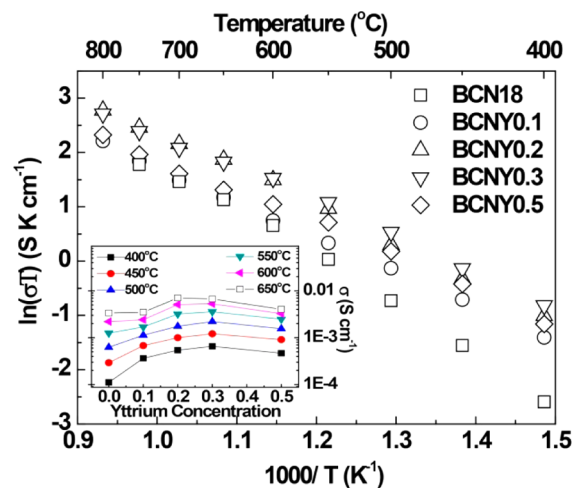


**Figure 4.** Arrhenius plots of the total conductivity of the samples in humidified air. The inset is the conductivity as a function of yttrium concentration.

Table 3. Conductivity and Stability Properties for Selected Proton Conductors

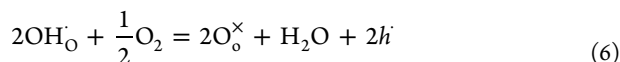
materials	conductivity @600 °C (S cm <sup>-1</sup> )	resistance to boiling water	resistance to pure CO <sub>2</sub>	resistance to CO <sub>2</sub> and water vapor <sup>a</sup>	reference
Ba <sub>3</sub> Ca <sub>1.18</sub> Nb <sub>1.52</sub> Y <sub>0.3</sub> O <sub>9-δ</sub>	5.3 × 10 <sup>-3</sup> , wet air	>24 h	>4 h @ 700 °C	>24 h @ 700 °C	this work
BaZr <sub>0.1</sub> Ce <sub>0.8</sub> Y <sub>0.1</sub> O <sub>3-δ</sub>	1.0 × 10 <sup>-2</sup> , wet H <sub>2</sub>		<2 h @ 900 °C		44
BaZr <sub>0.2</sub> Ce <sub>0.7</sub> Y <sub>0.1</sub> O <sub>3-δ</sub>		<6 h	<2 h @ 900 °C		45
BaZr <sub>0.3</sub> Ce <sub>0.5</sub> Y <sub>0.2</sub> O <sub>3-δ</sub>	4.5 × 10 <sup>-3</sup> , synth. air		<3 h @ 900 °C		46
BaZr <sub>0.4</sub> Ce <sub>0.4</sub> Y <sub>0.2</sub> O <sub>3-δ</sub>			<2 h @ 650 °C		47
BaZr <sub>0.45</sub> Ce <sub>0.45</sub> Sc <sub>0.1</sub> O <sub>3-δ</sub>	4.9 × 10 <sup>-4</sup> , amb. air		<1 h @ 900 °C		14
BaTa <sub>0.1</sub> Ce <sub>0.7</sub> Y <sub>0.2</sub> O <sub>3-δ</sub>		>3 h	>3 h @ 900 °C	<24 h @ 700 °C	48
BaIn <sub>0.2</sub> Ce <sub>0.7</sub> Y <sub>0.1</sub> O <sub>3-δ</sub>	5.0 × 10 <sup>-3</sup> , wet air			<24 h @ 700 °C	49

<sup>a</sup>The tests were conducted under 3% CO<sub>2</sub>+3% H<sub>2</sub>O balanced with air.

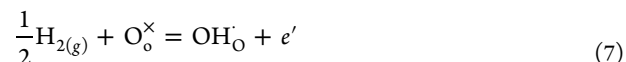
AC impedance measurement of the samples in wet air (3 vol % H<sub>2</sub>O) between 400 and 800 °C. From Figure 4 the activation energy  $E_a$  can be obtained from the slope of the Arrhenius plot through Arrhenius equation

$$\sigma T = A \exp\left(-\frac{E_a}{RT}\right) \quad (4)$$

where  $A$  is the pre-exponential factor proportional to the charge carrier concentration and  $E_a$  is the activation energy associated with the transport mechanism of the charge carriers. The activation energy values for the samples are  $0.75 \pm 0.02$ ,  $0.55 \pm 0.01$ ,  $0.59 \pm 0.01$ ,  $0.54 \pm 0.01$ , and  $0.52 \pm 0.01$  eV for BCN18, BCNY0.1, BCNY0.2, BCNY0.3, and BCNY0.5, respectively, showing a decrease with Y doping. As shown in the inset in Figure 4, the conductivity increases with Y concentration reaching 0.3 and then decreasing with  $x = 0.5$ , with BCNY0.3 showing the highest conductivity of  $5.3 \times 10^{-3}$  S cm<sup>-1</sup> at 600 °C in wet air, a value with 2.4 times improvement compared to undoped BCN18 ( $2.2 \times 10^{-3}$  S cm<sup>-1</sup> at 600 °C). This value is also comparable to the state-of-the-art Zr-doped BaCeO<sub>3</sub>-based materials. Table 3 compares the conductivity properties for BCNY0.3 and Ba(Zr,Ce)O<sub>3</sub> based materials. It can be seen that BCNY0.3 shows higher conductivity than BaZr<sub>0.3</sub>Ce<sub>0.5</sub>Y<sub>0.2</sub>O<sub>3-δ</sub> while it exhibits much better stability toward CO<sub>2</sub> or water. The activation energy of the total conductivity is influenced by the charge carriers existing in both bulk (grain) and grain boundary regions of the samples. For proton conductors, the main charge carriers are proton defects, which are formed mainly via eq 1. The protons (-OH group) are rotationally diffused, hopping between adjacent oxygen ions within the perovskite structure and leading to long-range proton conduction without movement of oxygen ions. Besides proton defects, there are also other charge carriers such as electronic holes ( $h$ ) and electrons ( $e'$ ). Under high oxygen partial pressure, p-type conduction represented in reactions 5 and 6 will be favored



Consequently, an increase in the oxygen partial pressure will result in consumption of oxygen vacancies and proton defects, leading to a decrease in proton conductivity or an increase in electronic conductivity. In the presence of very reducing atmospheres such as in dry hydrogen, hydrogen will react with oxide ions in the lattice producing hydroxide groups and electrons through reaction 7



In addition, under reducing environment, oxygen may leave the lattice creating oxygen vacancies and electrons as expressed in reaction 8



The temperature also affects the movement of the defects. As can be seen in Figure 4, with the increase in testing temperature, the conductivity increases almost linearly in the Arrhenius plot due to the increased mobility of proton defects in a thermally activated process.<sup>41</sup> At higher temperatures (>600 °C) the activation energy decreases slightly due to the occurrence of water desorption in the structure, resulting in a decrease in the proton concentration. The electronic hole or oxygen ionic conduction appear and are expected to dominate when temperature further increases.<sup>42</sup>

The measured conductivity in Figure 4 is the total conductivity of the materials, to which both bulk and grain boundary conduction contribute, whereas the bulk conductivity reflects the intrinsic properties of the materials. The bulk and grain boundary (GB) conductivity can be separated at lower temperature regime by fitting with RC equivalent circuit to the impedance spectra.<sup>13</sup> Figure 5 shows the bulk

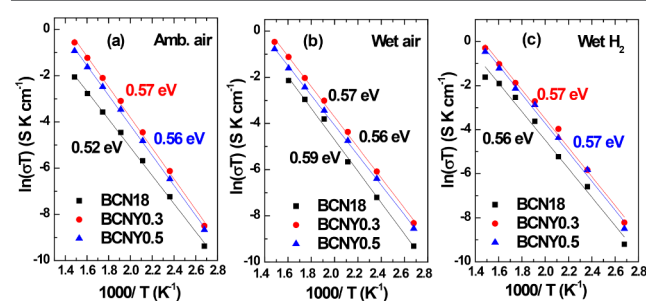


Figure 5. Bulk conductivity for selected samples measured at different atmospheres.

conductivity for selected samples in different atmospheres. Overall, it can be seen that BCNY0.3 shows the highest bulk conductivity in all atmospheres, followed by BCNY0.5, whereas BCN18 shows the lowest bulk conductivity. This can be explained in accordance with previous results that the introduction of up to 30% yttrium into BCN18 (BCNY0.3) has resulted in more oxygen vacancies into the system while at the same time leading to less cation ordering of the structure and, hence, improved bulk proton conductivity. Further doping of Y for BCNY0.5 resulted in composition changes in the bulk

(Ba evaporation), and the sample consequently showed lower bulk proton conductivity. The possible  $V_{\text{O}}^{\bullet\bullet}Y_{\text{Nb}}^{\prime\prime}$  clustered defects due to the excessive amount of  $V_{\text{O}}^{\bullet\bullet}$  in the bulk may also affect the effective oxygen vacancy amount and cause lower bulk conductivity. The activation energy for the bulk conduction ranges from 0.52 to 0.59 eV, characteristic of proton conduction.

Figure 6 shows the bulk and grain boundary (GB) conductivity for sample BCNY0.3 measured at the low temperature

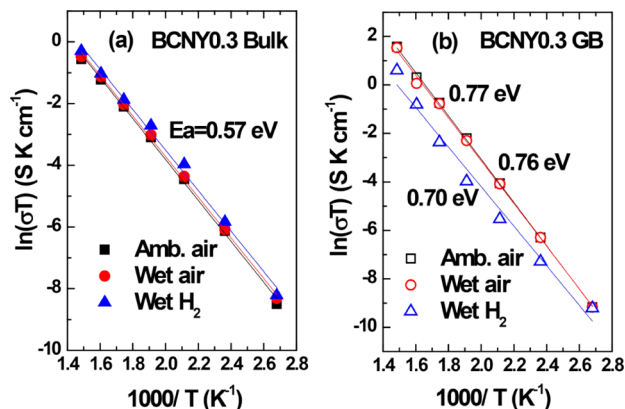


Figure 6. Bulk and grain boundary (GB) conductivity for BCNY0.3 at different atmospheres.

regime (from 100 to 400 °C) in ambient air, wet air, and wet H<sub>2</sub>, respectively. From Figure 6a it can be seen that the bulk conductivity changes as a function of oxygen partial pressure. The bulk conductivity in wet air and wet H<sub>2</sub> is higher than that in ambient air, which is indicative of proton conduction in the bulk area due to the introduction of water and hydrogen, respectively. Activation energy of 0.57 eV is also characteristic of proton conduction. For the grain boundary conductivity, the sample in wet H<sub>2</sub> shows a lower GB conductivity than in wet air and ambient air, indicating that protons are not the dominant charge carriers in the grain boundary area. Rather, p-type (electronic hole) conduction should appear at higher oxygen partial pressure based on the reactions 5 and 6. Higher activation energy in air than in H<sub>2</sub> (0.77 vs 0.70 eV) for BCNY0.3 is also indicative of the enhancement of electronic hole conduction.

**3.3. Chemical Stability.** To investigate the chemical stability of the Y-doped BCN18 compounds, the sintered pellets were ground into powders and then exposed to boiling water for 24 h. The treated powders were then examined by XRD, as shown in Figure 7. The XRD pattern of  $\text{BaZr}_{0.1}\text{Ce}_{0.7}\text{Y}_{0.1}\text{O}_{3-\delta}$  (BZCYYb) powder treated in boiling water for 4 h was compared as a reference. As shown in Figure 7, simple perovskite structure  $\text{BaCeO}_3$ -based proton conductors readily decompose in boiling water to form  $\text{Ba}(\text{OH})_2$  and  $\text{CeO}_2$  or react with  $\text{CO}_2$  in the air to form  $\text{BaCO}_3$ .  $\text{BaCeO}_3$  decomposed into the prevalent  $\text{CeO}_2$  and  $\text{BaCO}_3$  impurity phase, whereas  $\text{Ba}(\text{OH})_2$  was dissolved in water. For complex perovskite-structured BCN18-based proton conductors, they retained the perovskite structure without detectable impurities after exposure in boiling water for 24 h. It is clear that BCN18-based proton conductors are thermodynamically more stable than BZCYYb when treated in boiling water, and the introduction of yttrium did not show any detrimental effect on the chemical stability.

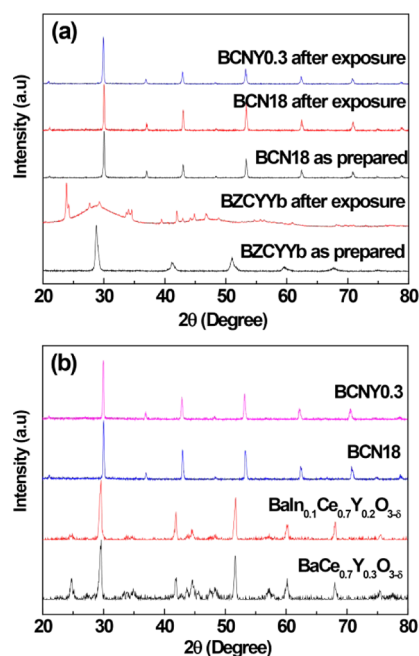
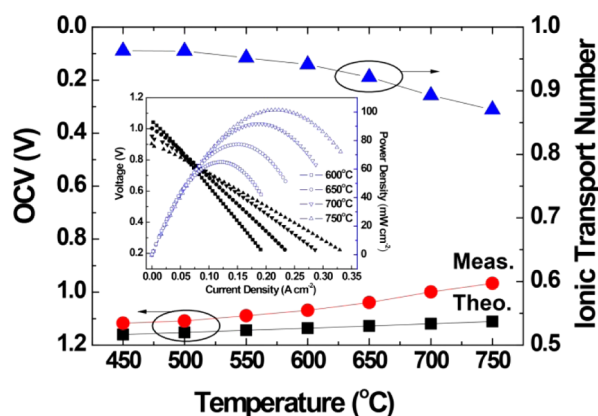


Figure 7. (a) XRD patterns of BCN18 and BCNY0.3 sample powders after exposure to boiling water for 24 h. The XRD pattern of BZCYYb powder treated in boiling water for 4 h is presented as reference. (b) XRD patterns of the sintered pellets after exposure to air with 3%  $\text{CO}_2$  + 3%  $\text{H}_2\text{O}$  at 700 °C for 24 h; the XRD patterns of  $\text{BaCe}_{0.7}\text{Y}_{0.2}\text{O}_{3-\delta}$  and  $\text{BaIn}_{0.1}\text{Ce}_{0.7}\text{Y}_{0.2}\text{O}_{3-\delta}$  powder treated in the same condition are presented as reference.

The stability of Y-doped BCN18 toward  $\text{CO}_2$  atmosphere also showed little change in terms of crystal structure. The sintered pellets were exposed to air containing 3 vol%  $\text{CO}_2$  and 3 vol%  $\text{H}_2\text{O}$  at 700 °C for 24 h. The XRD patterns of the surfaces of the pellets were collected after the treatments as shown in Figure 7b. No secondary phases can be observed for the differently treated BCN18 sintered pellets in all the XRD patterns, consistent with the reports for BCN18-based system.<sup>5,43</sup> Stability tests on  $\text{BaCe}_{0.7}\text{Y}_{0.2}\text{O}_{3-\delta}$  and  $\text{BaIn}_{0.1}\text{Ce}_{0.7}\text{Y}_{0.2}\text{O}_{3-\delta}$  samples were also included for comparison, both of which showed decomposition. The BCN18-based samples treated in pure  $\text{CO}_2$  at 700 °C extreme condition did not show any observable phase decomposition and secondary phase formation (see Supporting Information Figure S7). Thermogravimetry results in  $\text{CO}_2$  atmosphere also confirmed the chemical stability in  $\text{CO}_2$  gases (see Supporting Information Figure S8). Water and  $\text{CO}_2$  stability test results suggest that the Y-doped BCN18 samples showed sufficient chemical stability even in harsh conditions and the stability is not affected by the yttrium doping concentration up to 0.3. Table 3 also compares the chemical stability properties for selected samples. It can be seen that BCNY0.3 shows very promising chemical stability among the reported intermediate temperature perovskite proton conductors and acceptable conductivity compared with that of the state-of-the-art  $\text{Ba}(\text{Zr,Ce})\text{O}_{3-\delta}$ -based proton conductors.

**3.4. Electrochemical Characterization.** To determine the ionic transport number of the materials, the theoretical and measured open circuit voltage (OCV) values for BCNY0.3 with the configuration of 3 vol %  $\text{H}_2\text{O}-\text{H}_2/\text{Pt} \mid \text{BCNY0.3} \mid \text{Pt}/\text{Air}$  were obtained and are shown in Figure 8. The effective ionic transport number  $T$  can be calculated from

$$T = \text{OCV}_{\text{Meas.}} / \text{OCV}_{\text{Theor.}} \quad (9)$$



**Figure 8.** Theoretical and measured OCV values for BCNY0.3 with 3 vol %  $\text{H}_2\text{O}-\text{H}_2/\text{Pt} \mid \text{BCNY0.3} \mid \text{Pt}/\text{Air}$  and ionic transport number. Inset is the Power density as a function of current density performance for the Ni-BZCYYb  $\mid$  BCNY0.3  $\mid$  BCFN single cell.

where  $\text{OCV}_{\text{Meas.}}$  is the measured OCV and  $\text{OCV}_{\text{Theor.}}$  represents theoretical OCV calculated from the Nernst equation. It can be seen that an almost pure ionic behavior is observed at lower temperatures. The conducting ionic species are considered as protons because the material is proton conducting under low temperatures and wet  $\text{H}_2$  atmospheres. The deviation of  $\text{OCV}_{\text{Meas.}}$  from  $\text{OCV}_{\text{Theor.}}$  increases with temperature, especially at temperatures higher than 600 °C, indicating that the ionic transport number decreases with increasing operating temperature, demonstrating decreased proton conductivity and the increased influence of electronic conductivity at higher temperatures. This phenomenon can be understood through eqs 5 and 7, where electronic and proton mixed conductions appear at anode and cathode interface. In this case, the materials may be suitable for intermediate temperature SOFC application where pure ionic conduction is needed and for high temperature hydrogen separation membranes where proton/electronic mixed conduction is preferred.

The materials application has been demonstrated by the fabrication of proton-conducting solid oxide fuel cells with the cell configuration of Ni-BZCYYb  $\mid$  BCNY0.3  $\mid$  BCFN. Ni-BZCYYb was adopted as anode and BCFN was chosen as cathode because of their excellent electrochemical catalytic activity and good chemical stability.<sup>2,50</sup> The fuel cells were fabricated by a novel two-step cosintering method as reported elsewhere.<sup>33</sup> Inset in Figure 8 shows the I–V curves and power density of the fuel cell under different temperatures. Maximum power densities of 65, 77, 92, and 102  $\text{mW cm}^{-2}$  with OCV values of 1.04, 1.00, 0.95, and 0.90 V were achieved at 600, 650, 700, and 750 °C, respectively. The OCV values are consistent with the values obtained from the cell configuration using Pt as electrodes as shown in Figure 8. The electrochemical performance demonstrated the feasibility of electrochemical devices and further enhancements in fuel cell performance can be achieved by choosing suitable electrodes for the electrolyte membrane.

#### 4. CONCLUSIONS

Novel complex perovskite-structured  $\text{Ba}_3\text{Ca}_{1.18}\text{Nb}_{1.82-x}\text{Y}_x\text{O}_{9-\delta}$  proton conducting materials have been synthesized and characterized. Neutron powder diffraction and HRTEM determined the crystal structure as well as the cation ordering of the materials. Partial substitution of Nb by Y effectively

introduced more oxygen vacancies and reduced the degree of cation ordering, leading to increased ionic carrier concentration, mobility of the carriers, and consequently improved proton conductivity, specifically in the bulk areas. The optimum composition was determined to be  $\text{Ba}_3\text{Ca}_{1.18}\text{Nb}_{1.52}\text{Y}_{0.3}\text{O}_{9-\delta}$ , which possessed the highest proton conductivity among all the different Y doping concentrations and exhibited exceptional chemical stability toward water and  $\text{CO}_2$ , demonstrating a promising proton-conducting electrolyte material for intermediate temperature solid oxide fuel cells.

#### ■ ASSOCIATED CONTENT

##### Supporting Information

XRD XPS, thermodynamic calculations, SEM, and TG of the samples; impedance spectra and the cross-sectional microstructures of the fuel cell. This material is available free of charge via the Internet at <http://pubs.acs.org>.

#### ■ AUTHOR INFORMATION

##### Corresponding Author

\*F. Chen. Tel.: 803-777-4875. E-mail: [chenfa@cec.sc.edu](mailto:chenfa@cec.sc.edu).

##### Notes

The authors declare no competing financial interest.

#### ■ ACKNOWLEDGMENTS

This work was supported as part of the HeteroFoaM Center, an Energy Frontier Research Center funded by the U.S. Department of Energy, Office of Science, Basic Energy Sciences under Award # DE-SC0001061. S. Wang acknowledges support from the Student Stimulus Grant from the HeteroFoaM Center. S. Fang acknowledges support from the U.S. Department of Energy—Nuclear Energy University Program (NEUP). Y. Chen thanks the financial support from Materials Science and Engineering Division, Office of Basic Energy Sciences, Office of Science, U.S. Department of Energy for the part of the neutron work. The Research at Oak Ridge National Laboratory's Spallation Neutron Source was sponsored by the Scientific User Facilities Division, Office of Basic Energy Sciences, U.S. Department of Energy.

#### ■ REFERENCES

- (1) Iwahara, H.; Esaka, T.; Uchida, H.; Maeda, N. *Solid State Ionics* **1981**, 3–4, 359.
- (2) Yang, L.; Wang, S.; Blinn, K.; Liu, M.; Liu, Z.; Cheng, Z.; Liu, M. *Science* **2009**, 326 (5949), 126.
- (3) Kreuer, K. D. *Annu. Rev. Mater. Res.* **2003**, 33 (1), 333.
- (4) Pergolesi, D.; Fabbri, E.; D'Epifanio, A.; Di Bartolomeo, E.; Tebano, A.; Sanna, S.; Licocchia, S.; Balestrino, G.; Traversa, E. *Nat. Mater.* **2010**, 9 (10), 846.
- (5) Wang, S.; Zhao, F.; Zhang, L.; Brinkman, K.; Chen, F. J. *Power Sources* **2011**, 196 (19), 7917.
- (6) Wu, J.; Davies, R. A.; Islam, M. S.; Haile, S. M. *Chem. Mater.* **2005**, 17 (4), 846.
- (7) Amsif, M.; Marrero-Lopez, D.; Ruiz-Morales, J. C.; Savin, S. N.; Gabbás, M.; Nunez, P. J. *Power Sources* **2011**, 196 (7), 3461.
- (8) Tao, Z.; Zhu, Z.; Wang, H.; Liu, W. J. *Power Sources* **2010**, 195 (11), 3481.
- (9) Yan, L.; Sun, W.; Bi, L.; Fang, S.; Tao, Z.; Liu, W. J. *J. Alloys Compd.* **2010**, 508 (1), L5.
- (10) Zhao, F.; Wang, S.; Dixon, L.; Chen, F. J. *Power Sources* **2011**, 196 (18), 7500.
- (11) Wang, S.; Zhao, F.; Zhang, L.; Brinkman, K.; Chen, F. J. *J. Alloys Compd.* **2010**, 506 (1), 263.

- (12) Bi, L.; Zhang, S.; Fang, S.; Tao, Z.; Peng, R.; Liu, W. *Electrochem. Commun.* **2008**, *10* (10), 1598.
- (13) Wang, S.; Zhao, F.; Zhang, L.; Chen, F. *Solid State Ionics* **2012**, *213* (0), 29.
- (14) Azad, A. K.; Irvine, J. T. S. *Solid State Ionics* **2007**, *178* (7–10), 635.
- (15) Barison, S.; Battagliarin, M.; Cavallin, T.; Doubova, L.; Fabrizio, M.; Mortalo, C.; Boldrini, S.; Malavasi, L.; Gerbasi, R. J. *Mater. Chem.* **2008**, *18* (42), 5120.
- (16) Haugsrud, R.; Norby, T. *Nat. Mater.* **2006**, *5* (3), 193.
- (17) Kendrick, E.; Kendrick, J.; Knight, K. S.; Islam, M. S.; Slater, P. R. *Nat. Mater.* **2007**, *6* (11), 871.
- (18) Shin, J. F.; Hussey, L.; Orera, A.; Slater, P. R. *Chem. Commun.* **2010**, *46* (25), 4613.
- (19) Nowick, A. S.; Du, Y. *Solid State Ionics* **1995**, *77*, 137.
- (20) Du, Y.; Nowick, A. S. *Solid State Ionics* **1996**, *91* (1–2), 85.
- (21) Shimoyama, T.; Tojo, T.; Kawaji, H.; Atake, T.; Igawa, N.; Ishii, Y. *Solid State Ionics* **2008**, *179* (7–8), 231.
- (22) Nowick, A. S.; Du, Y.; Liang, K. C. *Solid State Ionics* **1999**, *125* (1–4), 303.
- (23) Deng, J.; Chen, J.; Yu, R.; Liu, G.; Xing, X. J. *J. Alloys Compd.* **2009**, *472* (1–2), 502.
- (24) Byeon, S.-H.; Lufaso, M. W.; Parise, J. B.; Woodward, P. M.; Hansen, T. *Chem. Mater.* **2003**, *15* (20), 3798.
- (25) King, G.; Thimmaiah, S.; Dwivedi, A.; Woodward, P. M. *Chem. Mater.* **2007**, *19* (26), 6451.
- (26) Burbano, M.; Norberg, S. T.; Hull, S.; Eriksson, S. G.; Marrocchelli, D.; Madden, P. A.; Watson, G. W. *Chem. Mater.* **2011**, *24* (1), 222.
- (27) Database of Ionic Radii. <http://abulafia.mt.ic.ac.uk/shannon/ptable.php> (accessed February 10, 2014).
- (28) Casu, A.; Ricci, P. C. *J. Solid State Chem.* **2011**, *184* (11), 3028.
- (29) An, K.; Skorpenske, H.; Stoica, A.; Ma, D.; Wang, X.-L.; Cakmak, E. *Metall. Mater. Trans. A* **2011**, *42* (1), 95.
- (30) An, K. ORNL Report: VDRIVE—Data Reduction and Interactive Visualization Software for Event Mode Neutron Diffraction; Oak Ridge National Laboratory: Oak Ridge, TN, 2012; Vol. ORNL-TM-2012-621.
- (31) Laurson, A. C., Von Dreele, R. B., *General Structure Analysis System (GSAS)*. Los Alamos National Laboratory: Los Alamos, NM, 2000; Vol. LAUR 86–748.
- (32) Toby, B. J. *Appl. Crystallogr.* **2001**, *34* (2), 210.
- (33) Wang, S.; Zhang, L.; Yang, Z.; Zhang, L.; Fang, S.; Brinkman, K.; Chen, F. *J. Power Sources* **2012**, *215* (0), 221.
- (34) Wang, S.; Zhang, L.; Zhang, L.; Brinkman, K.; Chen, F. *Electrochim. Acta* **2013**, *87* (0), 194.
- (35) Cai, L.; Liu, Z.; An, K.; Liang, C. *J. Mater. Chem. A* **2013**, *1* (23), 6908.
- (36) Huang, K.; Tichy, R. S.; Goodenough, J. B. *J. Am. Ceram. Soc.* **1998**, *81* (10), 2565.
- (37) Varela, A.; Dios, S. d.; Parras, M.; Hernando, M. a.; Fernández-Díaz, M. T.; Landa-Cánovas, A. R.; González-Calbet, J. M. *J. Am. Chem. Soc.* **2009**, *131* (24), 8660.
- (38) Morata-Orrantia, A.; García-Martín, S.; Alario-Franco, M. Á. *Chem. Mater.* **2003**, *15* (1), 363.
- (39) Irvine, J. T. S.; Corcoran, D. J. D.; Canales-Vazquez, J. *Solid State Ionics* **2002**, *152–153*, 749.
- (40) Garcia-Martin, S.; King, G.; Urones-Garrote, E.; Nénert, G.; Woodward, P. M. *Chem. Mater.* **2010**, *23* (2), 163.
- (41) Fabbri, E.; Pergolesi, D.; Traversa, E. *Chem. Soc. Rev.* **2010**, *39* (11), 4355.
- (42) Viana, H. d. A. L.; Irvine, J. T. S. *J. Mater. Chem.* **2010**, *20* (39), 8506.
- (43) Trinh, T. T.; Thangadurai, V. *Electrochim. Acta* **2010**, *56* (1), 227.
- (44) Katahira, K.; Kohchi, Y.; Shimura, T.; Iwahara, H. *Solid State Ionics* **2000**, *138* (1–2), 91.
- (45) Zhong, Z. *Solid State Ionics* **2007**, *178* (3–4), 213.
- (46) Fabbri, E.; D’Epifanio, A.; Di Bartolomeo, E.; Licoccia, S.; Traversa, E. *Solid State Ionics* **2008**, *179* (15–16), 558.
- (47) Guo, Y.; Lin, Y.; Ran, R.; Shao, Z. *J. Power Sources* **2009**, *193* (2), 400.
- (48) Bi, L.; Zhang, S.; Fang, S.; Tao, Z.; Peng, R.; Liu, W. *Electrochem. Commun.* **2008**, *10* (10), 1598.
- (49) Zhao, F.; Liu, Q.; Wang, S.; Brinkman, K.; Chen, F. *Int. J. Hydrogen Energy* **2010**, *35* (9), 4258.
- (50) Yang, Z.; Yang, C.; Jin, C.; Han, M.; Chen, F. *Electrochem. Commun.* **2011**, *13* (8), 882.